Nanoscale

ROYAL SOCIETY
OF CHEMISTRY

PAPER
Hongli Zhu *et al.*
Ultralight, highly thermally insulating and fire resistant aerogel by
encapsulating cellulose nanofibers with two-dimensional MoS_2

NCNST

Nanoscale

PAPER

Check for updates

Ultralight, highly thermally insulating and fire resistant aerogel by encapsulating cellulose nanofibers with two-dimensional MoS$_2$†

Lei Yang, [a,b] Alolika Mukhopadhyay,[a] Yucong Jiao, [a] Qiang Yong, [b]
Liao Chen,[a] Yingjie Xing,[a] Jonathan Hamel [a] and Hongli Zhu ✱[a]

Thermally insulating materials, made from earth-abundant and sustainable resources, are highly desirable in the sustainable construction of energy efficient buildings. Cellulose from wood has long been recognized for these characteristics. However, cellulose can be a flammability hazard, and for construction this has been addressed *via* chemical treatment such as that with halogen and/or phosphorus, which leads to further environmental concerns. Fortunately, the structure of cellulose lends itself well to chemical modification, giving great potential to explore interaction with other compounds. Thus, in this study, cellulose nanofibers (CNFs) were nano-wrapped with ultrathin 1T phase molybdenum disulfide (MoS$_2$) nanosheets *via* chemical crosslinking, to produce an aerogel. Thermal and combustion characterization revealed highly desirable properties (thermal conductivity k = 28.09 mW m^{-1} K^{-1}, insulation R value = 5.2, limit oxygen index (LOI) = 34.7%, total heat release = 0.4 MJ m^{-2}). Vertical burning tests also demonstrated excellent fire retardant and self-extinguishing capabilities. Raman spectra further revealed that MoS$_2$ remained unscathed after 30 seconds of burning in a 1300 °C butane flame. Considering the inherently low density of this material, there is significant opportunity for its usage in a number of insulating applications demanding specific fire resistance properties.

Introduction

Flame retardant materials with thermally insulating properties are desired for modern building construction. Residential and commercial buildings consume 40% of the total energy in the United States,[1] with 33% used for heating and 7% for cooling.[2] In 2008, fire departments responded to 378 600 home structure fires in the US[3] and fire accidents caused 16 705 civilian injuries, 3320 civilian deaths, and $138 billion in direct damage.[3] Typically, building insulation is produced from flammable organic and petroleum-derived polymers, including polystyrene,[4] urethane,[5] polyethylene,[6] chitosan[7] and cellulose.[8] Although these polymers are often manufactured with flame retardant additives, such as halogen[9] and phosphorus[10] to reduce flammability, the additives generate toxic products such as halogenated hydrogen and phosphorus oxide when burned.

Cellulose nanofiber (CNF), disintegrated from microfiber, has unique mechanical properties and provides renewable building blocks in materials with improved performance and new functionalities.[11–13] The cellulose aerogel is an excellent lightweight thermal insulator. However, the flammability of cellulosic materials introduced significant safety concerns with regard to their application in cellulose aerogels. Therefore, there is an urgent need to develop fire-resistant cellulose aerogels that are safe for use in energy-efficient buildings, transportation, and other applications. MoS$_2$ has relatively low thermal conductivity and good fire retardant characteristics with a high melting point of 1185 °C.[14–16] In a MoS$_2$/polymer composite, MoS$_2$ nanosheets create a nanobarrier which suppresses external heat and oxygen permeation and inhibits the release of volatile toxic substances.[15] Furthermore, the Mo atom accelerates charred layer formation within the polymer matrix,[17] thus improving the flame retardant characteristics of the polymer composite. MoS$_2$ exists in two phases: a semiconducting 2H phase and a metallic 1T phase. The tetragonal 1T phase is the more hydrophilic phase due to exposed Mo atoms,[18] and is thus more stable in water. The hydrophilicity of metallic MoS$_2$ plays a critical role in fabricating homogeneous nanocomposites in hydrophilic polymer matrices. Metallic MoS$_2$, however, does not occur naturally. In this work, we prepare metallic MoS$_2$ using a

[a]Department of Mechanical and Industrial Engineering, Northeastern University, Boston, Massachusetts 02115, USA. E-mail: h.zhu@neu.edu
[b]College of Chemical Engineering, Nanjing Forestry University, Nanjing, Jiangsu 210037, China
†Electronic supplementary information (ESI) available. See DOI: 10.1039/c7nr02243c

hydrothermal method, which is easier and safer than methods involving lithium intercalation into semiconducting MoS_2 with butyllithium.[18]

Dong *et al.* found that transition metal cations such as Fe^{3+}, Cu^{2+}, and Zn^{2+} effectively crosslink with carboxyl groups in CNF, allowing the formation of a three-dimensional polymer network.[19,20] Sathe *et al.* reported that Mo^{4+} is presented in MoS_2.[21] In metallic MoS_2, these surface cations can link with carboxyl (–COOH) and hydroxyl (–OH) groups in the cellulose chains to form cross-linked metal–carboxylate complexes. These complexes allow the MoS_2 nanosheets to effectively encapsulate the CNF in the nanoscale, based on which we prepared an ultra-light, highly porous aerogel with good mechanical strength by nanowrapping. Meanwhile, the aerogel exhibits excellent thermal insulation and fire resistance. The thermal conductivity of the aerogel is 28.09 mW m^{-1} K^{-1}, similar to that of air (26.2 mW m^{-1} K^{-1}). The limiting oxygen index (LOI) is 34.7%, which is 82.63% higher than that of pure cellulose (19%).[22] A vertical burning test (UL-94) further demonstrated the fire retardant and self-extinguishing capabilities of this aerogel. Cone calorimetry experiments utilizing the oxygen consumption principle resulted in a total heat release of 0.4 MJ m^{-2} of the CNF/MoS_2 aerogel. Furthermore, Raman spectra of the aerogel after burning confirmed that the MoS_2 remained stable. This lightweight, thermally insulated, and fire retardant aerogel can be useful in safe and energy efficient buildings and aerospace.

Results and discussion

In this work, CNF is prepared *via* a 2,2,6,6-tetramethyl-piperidine-1-oxyl radical (TEMPO) oxidation method. The obtained CNF disperses well in water, as shown in ESI Fig. 1a.† The C6-hydroxyl groups of the cellulose fiber surface were partially oxidized to carboxylate groups, which can cross-link with other polymers[23] and metal cations.[24,25] At a concentration of 1.5 wt%, the CNF slurry manifests as a gel, Fig. 1a. Two-dimensional MoS_2 nanosheets are prepared hydrothermally in an autoclave (Fig. 1b) with molybdenum trioxide and thioacetamide as precursors and urea as the reductant. Raman spectra (ESI Fig. 1b†) of the prepared MoS_2 contain peaks at 145, 213, and 321 cm^{-1}, which is a characteristic of the metallic phase MoS_2.[18] The black color of the MoS_2 slurry is further evidence of the metallic phase of the as-prepared MoS_2. Typically, semiconducting MoS_2 appears green as a result of the existence of a band gap. The trigonal octahedral structure of the 1T metallic phase MoS_2 is further illustrated in Fig. 1b. The prepared MoS_2 is highly hydrophilic with a contact angle of approximately 22° (ESI Fig. 1c†) and is extremely stable in water for at least 30 days (ESI Fig. 1d†). CNF is hydrophilic due to a high density of surface hydroxyl groups and carboxyl groups. No aggregation was observed during homogenization of the prepared CNF and MoS_2, and cross-linking of the MoS_2 and CNF by Mo^{4+}–carboxyl/hydroxyl bonding significantly promotes gelation of the solution.[26] Fig. 1c demonstrates the high viscosity of a 5 mg mL^{-1} CNF solution with 10.95 wt% MoS_2 added, with the underneath image further illustrating the crosslinking between MoS_2 sheets and CNF.[27] An ultra-light and freestanding nanocomposite aerogel (Fig. 1d) consisting of 2D MoS_2 nanosheet-wrapped CNF was prepared by freeze drying (see the Experimental section for more details). As illustrated in Fig. 1d, the individual cellulose 1D fiber provides the core for the ultrathin 2D MoS_2 nanosheets to wrap in the nanoscale. As is known, cellulose is highly flammable, but the protective layer of MoS_2 imparts excellent fire retardant properties to the aerogel.
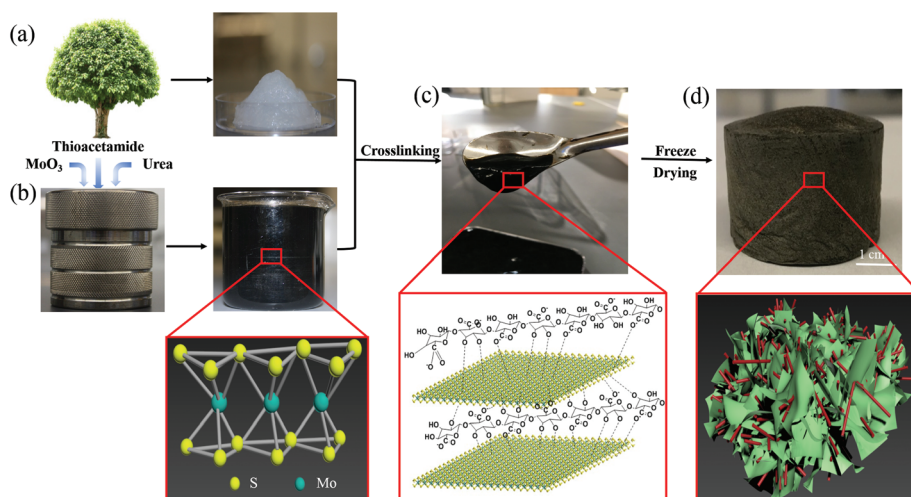

Fig. 1 (a) Cellulose nanofibers are disintegrated from hierarchical wood tracheid *via* chemical modification and mechanical homogenization. (b) 1T metallic phase MoS_2 nanosheets are synthesized by a hydrothermal process. The structure of the MoS_2 is depicted in the under red square. (c) Gelation of the CNF/MoS_2 hydrogel as a result of crosslinking between Mo^{4+} and –COOH, –OH groups on the cellulose chains. (d) Photograph of the as-prepared CNF/MoS_2 aerogel. The inset is a schematic representation of the composite aerogel structure with the MoS_2 nanosheets depicted in green sheet and the CNF in red fiber.
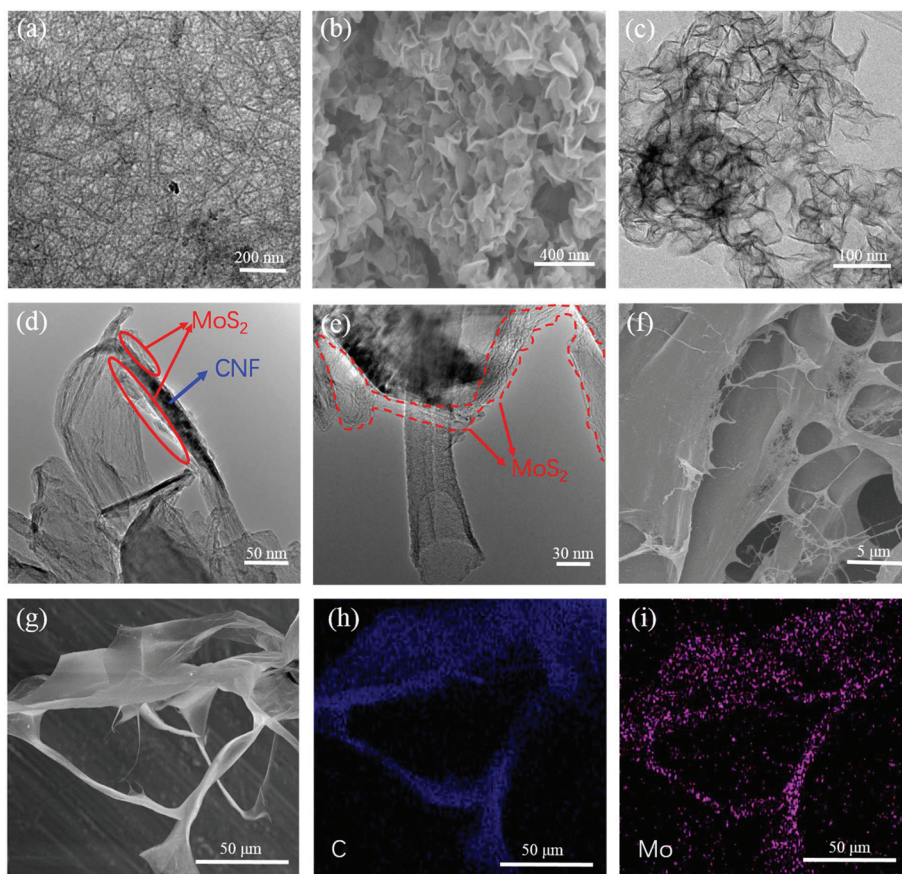
Fig. 2 (a) TEM image of CNF highlighting the nanofiber structure. (b) SEM and (c) TEM images of the morphology of the prepared metallic phase MoS$_2$ with a few layer, 2D nanosheet structure. (d), (e) TEM images of the CNF/MoS$_2$ mixture solution with the MoS$_2$ and CNF components marked. (f), (g) SEM images of the CNF/MoS$_2$ nanocomposite aerogel. Elemental maps of the region in (g) for carbon (h) and molybdenum(i).

Transmission electron microscopy (TEM) images of the morphology of the prepared CNF are presented in Fig. 2a. The CNF exhibits a uniform fibrous structure with ~10 nm wide and more than 400 nm long fibers. The morphology of MoS$_2$ was examined *via* a scanning electron microscope (SEM) in Fig. 2b and a TEM in Fig. 2c. The flaky lamellar structure presented in Fig. 2b is typical of MoS$_2$. The average planar size of the nanosheets is approximately 50 nm. Fig. 2c indicates that the MoS$_2$ nanosheets are at most a few layers thick. This morphology exposes a high density of Mo^{4+} cations for cross-linking with the CNF. The morphology of the CNF/MoS$_2$ nanocomposite mixture is shown in Fig. 2d and e. From Fig. 2d, it is apparent that MoS$_2$ nanosheets completely encapsulated the CNF. The 2D layered structure of MoS$_2$ nanosheets bound to the CNF framework is clearly defined in Fig. 2e. More images are provided in ESI Fig. 2a and b.† SEM images of the aerogel are provided in Fig. 2f and g. The aerogel consists of a large, integrated sheet structure with an abnormally shaped pore structure of the walls. Energy dispersive spectroscopy (EDS) elemental maps of C and Mo distributions in the region in Fig. 2g are presented in Fig. 2h and i, respectively. These elemental maps indicate that the MoS$_2$ are uniformly distributed on CNF within the aerogel.

The mass and volume of the prepared aerogels were accurately measured to calculate the density. As reported in ESI Table 1,† the density of the CNF/MoS$_2$ nanocomposite aerogel is 0.00473 g cm^{-3} and the density of the CNF aerogel is 0.00453 g cm^{-3}. Brunauer–Emmett–Teller (BET) characterization was performed on nitrogen absorption and desorption isotherms to determine the specific surface area. Isotherms on both the CNF and CNF/MoS$_2$ aerogels are presented in Fig. 3a. Both samples have type IV with an H3 hysteresis.[28] The specific surface areas were calculated to be 20.62 m^2 g^{-1} for the CNF aerogel and 10.60 m^2 g^{-1} for the CNF/MoS$_2$ nanocomposite aerogels (ESI Table 1†). The cumulative pore volumes of CNF and CNF/MoS$_2$ aerogels are 0.038 cm^3 g^{-1} and 0.026 cm^3 g^{-1} in the range of 1–216 nm and 1–136 nm individually. The pore size distribution, shown in Fig. 3b, was determined using the Barrett–Joyner–Halenda (BJH) method. These results indicate that the majority of pore diameters are in the range of 30–70 nm. The character of the porous structure significantly decreases the gas and solid conduction in the aerogel,[29] which in turn significantly improves thermal insulation. As presented in the SEM image in Fig. 3c, the CNF/MoS$_2$ aerogel contains pores of various sizes surrounded by thin films. X-ray microcomputed tomography (μCT) was further
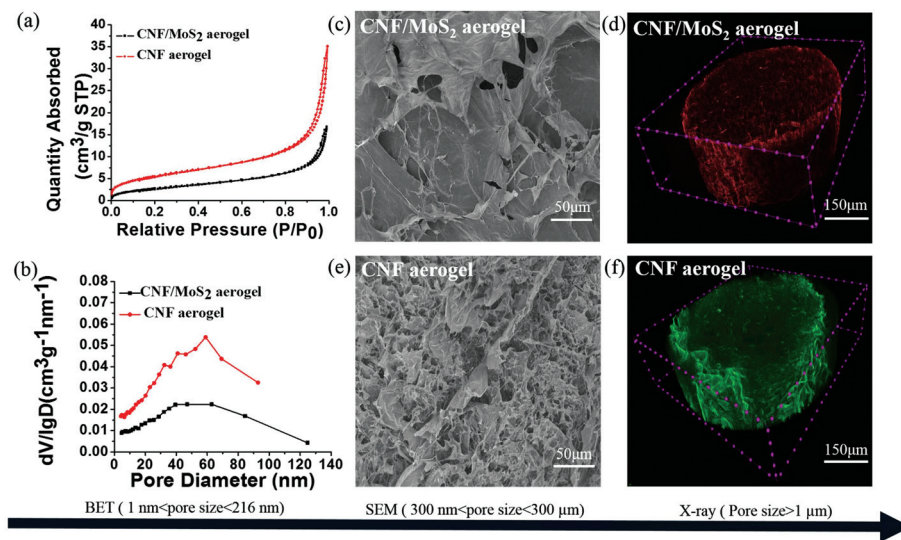
Fig. 3 (a) Nitrogen adsorption and desorption isotherms for CNF and CNF/MoS$_2$ aerogels. (b) BJH pore diameter analysis for CNF and CNF/MoS$_2$ aerogels. SEM images of the (c) CNF/MoS$_2$ aerogel and (e) CNF aerogel highlighting the difference in the pore structure. X-ray microcomputed tomography (μCT) reconstructions of the (d) CNF/MoS$_2$ nanocomposite aerogel with 80.44% porosity and the (f) CNF aerogel with 85.49% porosity.

used to investigate pores larger than 1 μm. The reconstructed structure of the CNF/MoS$_2$ nanocomposite aerogel is displayed in Fig. 3d and ESI Video 1.† The calculated porosity of pores higher than 1 μm is 80.44%. The SEM images of the CNF aerogel displayed small pores with no film, as presented in Fig. 3e. The pure CNF aerogel was also analyzed by X-ray μCT and a depiction is presented in Fig. 3f and ESI Video 2.†

SEM images highlighting the morphology and pore structure of the CNF/MoS$_2$ aerogel in the radial and axial directions are provided in Fig. 4a–c. From these images, it can be seen that the sheet-like, closed pore structure is similar in both directions. The viscosities of the MoS$_2$, CNF, and CNF/MoS$_2$ solutions were measured (see the Experimental section) and the results are plotted in Fig. 4d. The viscosity of the CNF/MoS$_2$ mixture (227.21 mPa s) is three times greater than that of the pure CNF solution (70.21 mPa s). The viscosity of the pure MoS$_2$ solution is 2.88 mPa s, similar to that of DI water. It is apparent that the high viscosity of the CNF/MoS$_2$ imparted by crosslinking is beneficial to aerogel formation. Note that with the same concentration of 5 mg mL^{-1}, it is impossible to create a stable pure CNF aerogel. In Fig. 4(e) and (f), the XPS spectra of MoS$_2$ and CNF/MoS$_2$ composite aerogels are investigated. The Mo 3d high-resolution spectrum of MoS$_2$, Fig. 4e, displays two characteristic peaks at 228.7 and 231.9 eV, which correspond to the Mo–S bond. In contrast, one new peak appearing at 235.9 eV in Fig. 4f is presented in the spectrum of the CNF/MoS$_2$ aerogel, which corresponds to the Mo–O bond.[30] This Mo–O bonding indicated the existence of the chemical crosslinking between Mo^{4+} cations, and carboxyl (–COOH), and hydroxyl (–OH) groups in the CNF/MoS$_2$ aerogel.

The freestanding mechanical properties of the CNF/MoS$_2$ nanocomposite aerogel are highlighted in Fig. 4g, where it can be seen that a 0.1 g aerogel sample supports a 210 g object, heavier than 2000 times its own weight, with no deformation.

The mechanical properties of the aerogel were further characterized by compression tests in both the radial and axial directions. The compression stress–strain curves are presented in Fig. 4h and i. The isotropic, sheet-like, porous structure apparent in Fig. 4a and b provides the aerogel with excellent mechanical strength in both directions. The aerogel can be compressed to 60% strain at relatively low stresses of 17.70 kPa in the radial direction and 24.98 kPa in the axial direction, demonstrating excellent elasticity. At 90% strain, the compressive stresses on the aerogel increase to 216.64 kPa in the radial direction and 215.85 kPa in the axial direction. This result is significantly higher than the reported values of 25.3 kPa for pure CNF aerogels.[31] Young's moduli of 299.23 kPa in the radial direction and 326.48 kPa in the axial direction were calculated and are plotted in Fig. 4i. The mechanical properties of the CNF/MoS$_2$ nanocomposite aerogel are a significant improvement over other CNF aerogels prepared at the same CNF concentration. The increase in strength is attributed to crosslinking between the Mo^{4+} cation, carboxyl, and hydroxyl groups on the CNF. The mechanical properties of the CNF/MoS$_2$ aerogel are nearly isotropic, consistent with the disordered sheet-like porous structure.

The limiting oxygen index (LOI) is the minimum oxygen concentration in an oxygen/nitrogen mixture that supports material combustion and serves as an important parameter in characterizing the performance of fire retardant materials, whereas, a higher LOI indicates better fire resistance capabilities.[32] In this work, the LOI is determined by following the ASTM 2863 standard using a FTT oxygen index test equipment as described in the Experimental section. The results of the experiment can be viewed in ESI Video 3.† The LOI of the CNF/MoS$_2$ composite aerogel is 34.7%, twice that of the pure cellulose (19%).[22] This LOI also exceeds the value for other cellulosic fire retardants, including cellulose/montmorillonite
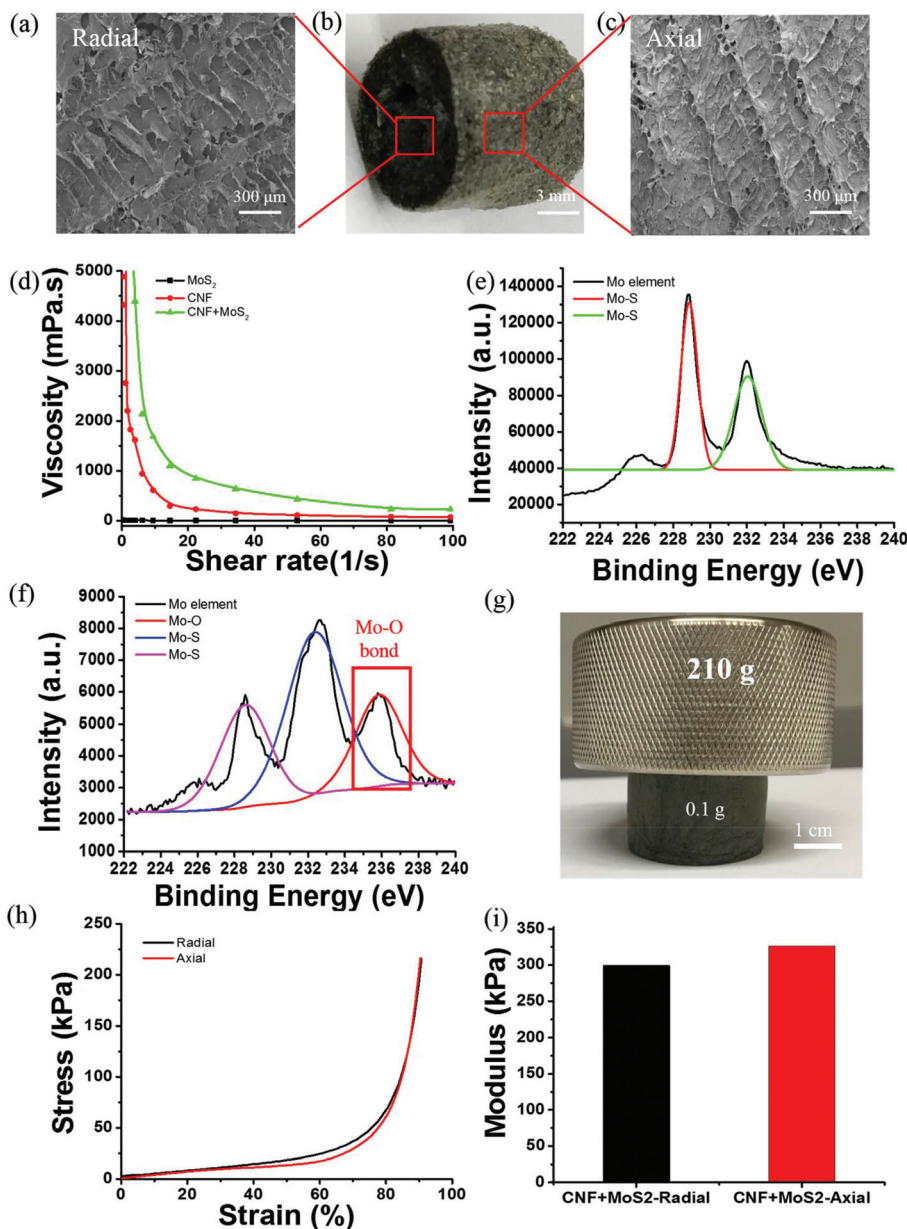
Fig. 4 SEM images of the CNF/MoS$_2$ nanocomposite aerogel in the (a) radial and (c) axial directions. (b) Digital photograph of the aerogel. (d) Plot of viscosity curves for MoS$_2$, CNF, and CNF/MoS$_2$ solutions. (c) XPS of the Mo 3d spectrum in MoS$_2$ before chemical crosslinking. (d) XPS of the Mo 3d spectrum in the CNF/MoS$_2$ composite aerogel after chemical crosslinking. (g) Digital image highlighting the strength of the aerogel, in which a 0.1 gram sample of the aerogel can support a 210 g weight. (h) Stress–strain curves of the CNF/MoS$_2$ nanocomposite aerogel in the radial and axial directions. (i) Young's moduli E of the aerogel in the radial and axial directions.

nanocomposites (29.3%)[32] and cellulose/magnesium hydroxide nanocomposite films (20%).[33] Wicklein and colleagues[34] have reported an LOI of 34% for nanocellulose/graphene oxide/magnesia silicate/boric acid foams, which is on par with our results.

The thermal conductivity coefficient of the CNF/MoS$_2$ nanocomposite aerogel was measured using a TPS 3500 hot disk instrument (Hot Disk AB, Sweden) at 22 °C. Further details and images are provided in ESI section 1.† The thermal conductivity of the aerogel is 28.09 mW m^{-1} K^{-1}, close to the

thermal conductivity of air (26.2 mW m^{-1} K^{-1}) at ambient temperature. The corresponding insulation R value per inch is 5.2. Cellulose has a thermal conductivity of 40 mW m^{-1} K^{-1} and an insulation R value per inch of about 3.5. Therefore our aerogel has better thermal insulation property. Thermal transmission in the aerogel is primarily due to three factors: heat conduction, convection, and radiation.[34] The majority pore size distribution of the aerogel (30–70 nm) is smaller than the mean free path of the gas (70 nm), which significantly decreases the gas heat conduction by the Knudsen effect.[35]

Additionally, the low density (0.0047 g cm^{-3}) and porous structure of the aerogel decrease heat conduction through the solid.[29] Thermographic images captured with an infrared camera (Fig. 5a and b) reveal that the CNF/MoS$_2$ nanocomposite aerogel is highly insulating in both the axial and radial directions. The temperature profile within the aerogel was modeled in the COMSOL Multiphysics software using the heat conduction equation given by:[36]

$$\rho c_p \frac{\partial T}{\partial t} + \nabla \cdot (k \nabla T) = 0 \tag{1}$$

where ρ is the density of the aerogel, c_p is the specific heat at constant pressure, k is the thermal conductivity as measured in the thermal conductivity experiment, t is the time, and T is the temperature of the aerogel. Boundary conditions at the aerogel boundary are given by:

$$k \left(\frac{\partial T}{\partial n} \right) = h(T - T_{ext}) \tag{2}$$

where n is the unit vector normal to the boundary; the temperature at the boundary between the aerogel and the hot plate is set to 70 °C; the natural convection heat transfer coefficient h is estimated at 0.5 W (m^2 K)$^{-1}$, and T_{ext} is set to an external ambient temperature of 20 °C. The temperature profile results plotted in Fig. 5c and d confirm the superior insulating capabilities of the aerogel.

A vertical burning test consistent with the UL 94 standard method was used to characterize the combustion behavior of the CNF/MoS$_2$ nanocomposite aerogel. The results, presented in Fig. 5e and ESI Video 4,† indicate that the aerogel displays excellent fire retardant and self-extinguishing properties. We attribute these properties to several beneficial effects of MoS$_2$ addition. The melting point of MoS$_2$ is 1185 °C,[16] providing the aerogel with excellent thermal stability at high temperature. Encapsulation of the CNF by MoS$_2$ nanosheets forms an excellent physical barrier to prevent CNF combustion. Zhou *et al.* reported that MoS$_2$ acting as a "char reinforcer" remarkably promotes polymer carbonization to the char layer, further improving the flame retardant properties.[37] The importance of the nanocomposite aerogel structure is confirmed by additional experiments. A control CNF/MoS$_2$ aerogel, prepared by dipping a CNF aerogel into a MoS$_2$ solution, was also subjected to the vertical burning test (ESI Video 5†). The control sample burned expeditiously and the structure nearly collapsed into a powder after burning. It is likely that this facile dipping process only coats the exterior surface of the aerogel with MoS$_2$ nanosheets. These results indicate the importance of MoS$_2$ crosslinking with CNF to encapsulate the CNF and form a protective barrier.

Thermogravimetric analysis (TGA) curves display the thermal degradation of CNF and CNF/MoS$_2$ aerogels in Fig. 5f. A clear difference is presented between the CNF and CNF/MoS$_2$ aerogels in the TGA curves. The TGA curve of the CNF aerogel shows the first stage of degradation temperature to be in the range of 240–320 °C, while the degradation temperature range of the CNF/MoS$_2$ aerogel significantly increased to the range of 300–400 °C due to the existence of MoS$_2$. Compared with the CNF aerogel sample, the weight loss of CNF/MoS$_2$ was reduced from ~80% to ~60%, which indicated that the thermal stability of the aerogel improved through MoS$_2$ nanosheets forming an excellent physical barrier to prevent the CNF aerogel from combustion. In Fig. 5g, the C 1s spectra of the CNF/MoS$_2$ aerogel after burning show three characteristic peaks at 284.98, 286.58 and 288.08 eV, which is ascribed to the binding energies of C–C, C–O and O–C=O bond, respectively. The O–C=O bonding (highlighted in the red square in Fig. 5g) is a typical bonding in TEMPO oxidized CNF. The residual O–C=O bonding after burning indicated that a large portion of the CNF aerogel was successfully protected from burning because of the external wrapping of 2D MoS$_2$.

The combustion behavior of the CNF/MoS$_2$ aerogel was further investigated by oxygen consumption cone calorimetry. Following ASTM standard E 1354, the aerogel was exposed to a 25 kW m^{-2} heat flux. Over the course of the test, depicted in Fig. 5h, there was limited ignition and no visible flame or smoke appeared. The results of the experiment are summarized in ESI Table 2† and compared with published results for carboxymethyl cellulose sodium (CMC).[38] The addition of sodium to CMC significantly improved the fire resistant properties of cellulosic materials. The peak heat release rate of the aerogel (pkHRR) during the experiment is 31 kW m^{-2}, as opposed to 60 kW m^{-2} for pure CNF aerogels,[34] and 94.4 kW m^{-2} for the CMC study. The total heat release (THR) of the CNF/MoS$_2$ aerogel is 0.4 MJ m^{-2}, again smaller than that of the CMC study (1.53 MJ m^{-2}).[38] These results demonstrate that the addition of MoS$_2$ remarkably suppresses the combustion of cellulosic materials. The CNF/MoS$_2$ nanocomposite aerogel shrank during the cone calorimetry test, but retained 82% of the initial mass. We expect that CNF on the exterior of the aerogel was carbonized to form a residual char layer, which acted as a protective barrier against further damage.

The morphology and structure of the aerogel were characterized after combustion. Macroscopically, the initial sheet structure is reduced to the fascicular structure seen in Fig. 6b and no apparent differences are observed in the microscopic structure in either the radial or axial directions (Fig. 6a and c). Smooth carbon sheets with a visibly intact char layer are highlighted by arrows in Fig. 6d. Feng *et al.*[39] have reported that the addition of MoS$_2$ can improve the ability of polymers to carbonize and form an intact char layer. Raman spectra of the CNF/MoS$_2$ nanocomposite aerogel post combustion are presented in Fig. 6e and f. In Fig. 6e, the peaks at 1358 cm^{-1} and 1586 cm^{-1} are attributed to the D and G bands of carbon, respectively, and indicate that the CNF was carbonized to form a thermally stable char layer. The formation of an intact protective char layer as a secondary physical barrier could further improve the thermal stability and fire retardant properties of the aerogel.[39] The TGA curve of the CNF/MoS$_2$ aerogel after burning shows a higher degradation temperature range (350–475 °C) and lower weight loss (~54%) than those of the CNF/MoS$_2$ aerogel before burning, in ESI Fig. 3.† These results
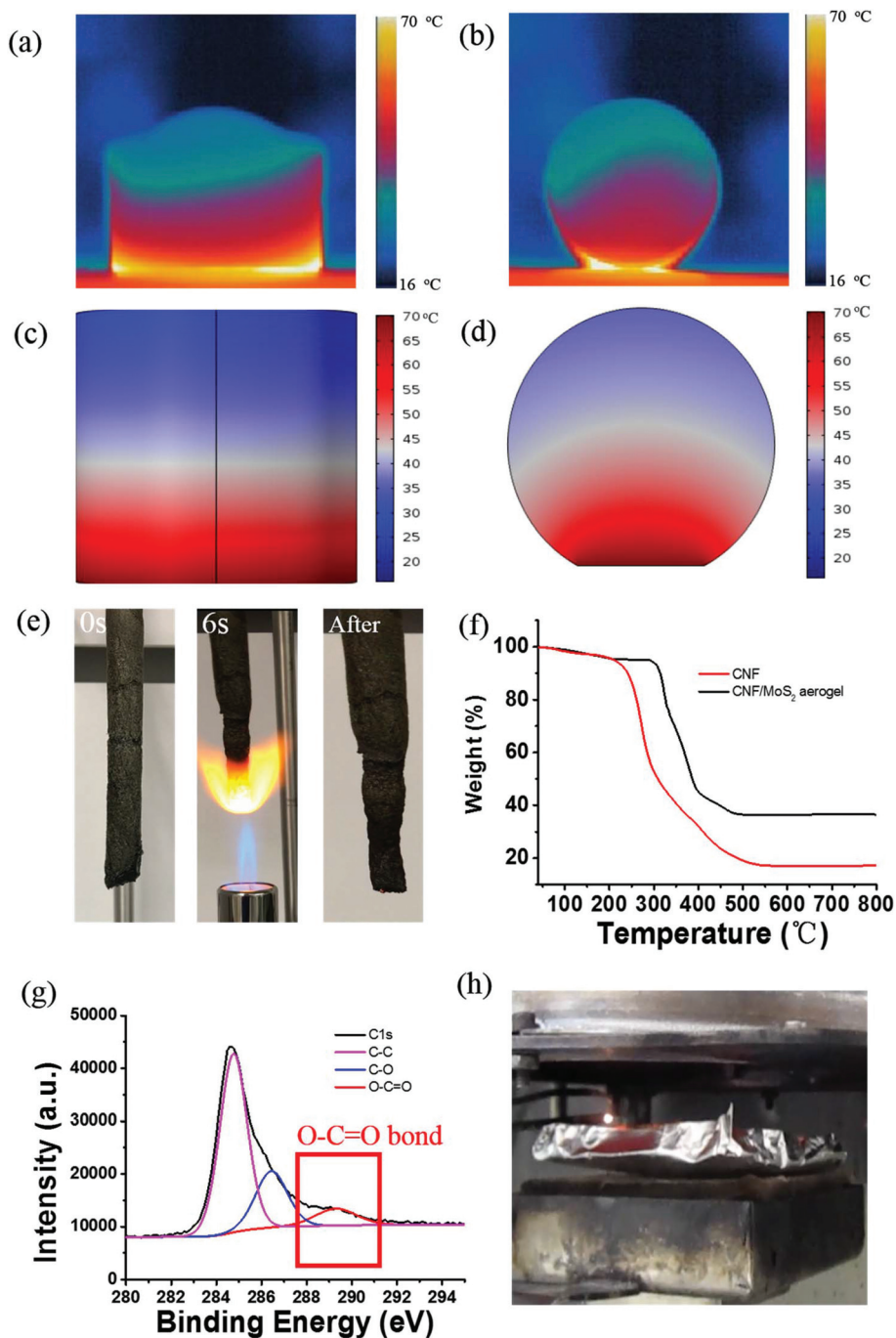
Fig. 5 Thermographic images and temperature distributions in the CNF/MoS$_2$ nanocomposite aerogel in the (a) axial and (b) radial directions. Results of temperature profile modeling in the (c) axial and (d) radial directions. (e) Combustion behavior of the CNF/MoS$_2$ nanocomposite aerogel during the vertical burning test. From left to right, digital images of the aerogel before the flame is applied, after 6 seconds of exposure to a 1300 °C butane flame, and after the flame is removed. (f) TGA curves of CNF and CNF/MoS$_2$ aerogels. (g) XPS of C 1s spectra in CNF/MoS$_2$ aerogels after burning. (h) Photograph of the CNF/MoS$_2$ nanocomposite aerogel during the cone calorimetry test, which no sustainable flame was observed.

further confirmed that the formation of an intact protective char layer as a secondary physical barrier could improve the thermal stability of aerogels.

Raman spectra for MoS$_2$ in the CNF/MoS$_2$ nanocomposite aerogel before and after burning are presented in Fig. 6f. From

the existence of the characteristic E$_{2g}^1$ and A$_{1g}$ peaks located at ~378 cm^{-1} and ~403 cm^{-1} in the spectrum obtained after burning, we conclude that the MoS$_2$ remained after burning. Note that compared to the Raman spectrum of MoS$_2$ immediately after synthesis (ESI Fig. 1b†), we noticed that the MoS$_2$
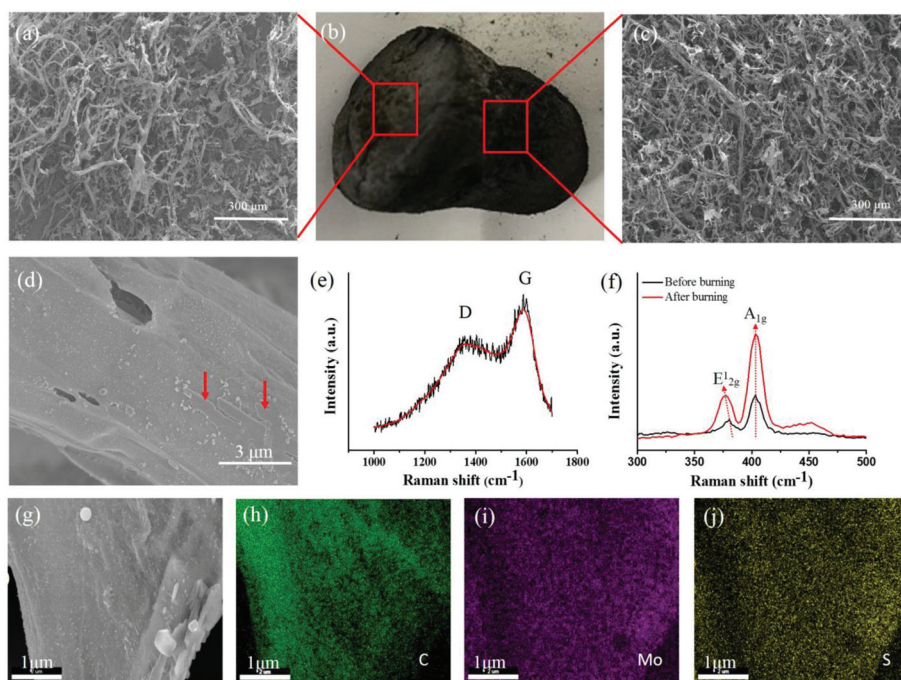
Fig. 6 SEM images from the (a) radial and (c) axial faces of the CNF/MoS$_2$ nanocomposite aerogel after burning. (b) Digital photograph of the aerogel after burning. (d) SEM image of the aerogel surface after burning at 1300 °C butane flame. The char layer is indicated by red arrows. (e) and (f) Raman spectra of the aerogel after burning. (g) SEM image of the aerogel after burning with corresponding elemental maps for (h) carbon, (I) molybdenum, and (j) sulfur.

changed from the 1T phase to the 2H phase. This might be attributed to the external vacuum force during the freeze-drying process. The peak separation between the E_{2g}^1 and A_{1g} modes is narrower for the aerogel than what is reported for pure semiconducting MoS$_2$, which indicates that the thickness of the MoS$_2$ layer decreased during processing. It is likely that the existence of CNF in solution further contributed to the dispersion of the MoS$_2$.[40] After burning, the E_{2g}^1 peak shifted to 376 cm^{-1} and the A_{1g} peak shifted to 403 cm^{-1}. This increase in peak separation indicates that the MoS$_2$ layers thickened during the burning process. This phenomenon is consistent with the SEM images provided in Fig. 6a and c, in which a crinkling of the structure is observed after combustion. Additionally, EDS maps of the aerogel after combustion are presented in Fig. 6g–j. The distribution of carbon in Fig. 6h is a result of both the CNF and char. Based on the consistent distribution of Mo and S in Fig. 6i and j, we conclude that MoS$_2$ remaining in the combustion residue stayed stable after burning.

Conclusion

In summary, for the first time, we prepared a unique nanocomposite aerogel consisting of a CNF skeleton encapsulated by a layer of ultrathin, fire retardant metallic MoS$_2$ nanosheets. The strong bonding between the nanosheets and nanofibers is a result of chemical crosslinking between Mo^{4+} cations,

carboxyl (–COOH), and hydroxyl (–OH) groups in the cellulose. This crosslinking increased the viscosity of the hydrogel mixture, allowing the formation of an aerogel with 97.36% porosity and 0.00473 g cm^{-3} density. The aerogel exhibits excellent fire resistant properties, including a thermal conductivity of 28.09 mW m^{-1} K^{-1} (insulation R value per inch of 5.2), oxygen index of 34.7%, and a total heat release of 0.4 MJ m^{-2} as characterized by cone calorimetry utilizing the oxygen consumption principle. A vertical burning test demonstrated the excellent fire resistant and self-extinguishing capabilities of the aerogel. Raman spectra of the aerogel after the vertical burning test confirmed that the MoS$_2$ structure remained stable. This work provides a novel strategy to prepare a lightweight, highly thermally insulating, and fire resistant aerogel for construction of fire resistant and energy efficient buildings and for application in aerospace.

Experimental section

MoS$_2$ preparation

1.2 mg per mL of molybdenum trioxide (Sigma-Aldrich, USA), 1.4 mg per mL of thioacetamide (Sigma-Aldrich, USA) and 10 mg per mL of urea (Fisher Scientific, USA) were mixed with DI water using a magnetic stirrer. The mixture is then poured into an autoclave (Parr Instrument Cop. USA) and reacted at 200 °C for 18 h. The product was repeatedly washed with both ethanol and DI water and sonicated in an ultrasonic generator

(Boston LabCo, USA) with an amplitude of 20% for 10 min to obtain 2D nanolayered MoS_2.

Cellulose nanofiber fabrication

The cellulose nanofibers were prepared from softwood pulp, 2 g of softwood pulp was added to 100 mL DI water containing 0.032 g of TEMPO (Sigma-Aldrich, USA), 0.2 g of NaBr (Sigma-Aldrich, USA) and 6 mL of 12.5 wt% NaClO solution (Sigma-Aldrich, USA). 0.5 mol L^{-1} NaOH was added to maintain pH 10.0 at ambient temperature. After 2 h, the pH of the resulting mixture showed no further change, and the reaction was terminated. The oxidized cellulose fibers were sufficiently washed, and then the solid portion was sonicated in an ultrasonic generator with an amplitude of 40% for 60 min.

Aerogel preparation

5 mg mL^{-1} of oxidized cellulose nanofibers were completely suspended in DI water and mixed with 10.95 wt% of 2D nanolayered MoS_2 using an ultrasonic generator; the mass ratio of cellulose and MoS_2 is 8.13 : 1. The CNF/MoS_2 mixture was degassed under a vacuum and left to stand, to allow for cross-linking, then the mixture was slowly poured into a cylindrical Teflon mold and quickly frozen in a liquid nitrogen bath. It was then dried to form the aerogel in a freeze dryer (Labconco).

Transmission electron microscopy observations

TEM and HRTEM imaging were performed on a FEI Tecnai G2 F20 S-Twin microscope (FEI Company, USA) and the instrument voltage set to 100 kV. The sample was sonicated, diluted and centrifuged, then 25 μL supernatant was dropped and dried onto holey carbon grids.

Scanning electron microscopy observations

The morphology of the aerogels was measured by using a ultra-high resolution scanning electron microscope (Hitachi S4800, USA). The aerogel samples were obtained in the radial and axial directions. Then the samples were coated with 5 nm platinum and measured under ultra-high resolution mode with 3 kV accelerating voltage.

Raman spectroscopy

Raman spectroscopy was performed with 532 nm laser excitation using a LabRam HR800 UV NIR (Horiba Scientific, USA). The samples were measured using silicon substrates as the sample holder.

Surface area and pore size distribution test

The surface area of the aerogel was studied on a TriStar II 3020 surface area analyzer (Micromeritics Instruments) by using N_2 gas adsorption at 77 K. The surface area was calculated according to the Brunauer–Emmett–Teller (BET) analysis method. The pore size distribution was calculated from the desorption branch of the isotherm curve according to the Barret–Joyner–Hallender (BJH) method.

X-ray tomography observations

Cylindrical samples (10 × 10 mm) were prepared for the X-ray tomography. The samples were loaded and tested on a rotating plate, the X-ray sources were set at 47 kV, 213 μA and 10 W, the 2D images were collected by using a planar multichannel X-ray detector. The 2D images were reconstructed in the NRecon software, the porosity of sample was measured in the CTan analyser software.

X-ray photoelectron spectroscopy test

XPS was characterized by an Axis Ultra DLD (Kratos Analytical, UK) system. A monochromatic aluminum Kα source was used at 150 W power. The pass energy of the wide scan and narrow scan was set at 160 eV and 40 eV, respectively.

TGA test

The TGA measured the degradation property of CNF and CNF/MoS_2 aerogel by using a Netzsch STA 409 PC (TGA instrument, Germany). The samples were heated in air with a heating rate of 10 °C min^{-1}. The test temperature was set at a range from 40 to 800 °C.

Viscosity test

The solution viscosity of MoS_2 (0.615 g L^{-1}), CNF (5 g L^{-1}) and the CNF/MoS_2 mixture (5 g L^{-1} CNF and 0.615 g L^{-1} MoS_2) was measured by using a Discovery HR-2 Rheometer (TA instrument, USA) at 25 °C. The samples were measured at shear rates from 0.01 to 100 s^{-1}.

Mechanical properties test

The compressive mechanical properties of the aerogel was investigated using a Discovery HR-1 Rheometer (TA instrument, USA). The radial and axial directions of the cylindrical aerogel (17 mm diameter) were obtained from the large bulk aerogel and the compression rate was set at 1.0 N min^{-1}. The compressive Young's modulus was calculated according to the stress *versus* strain curve in the linear range.

Thermal conductivity properties and thermographic images

The thermal conductivity properties were measured by using a Hot Disk TPS 3500 instrument (Hot Disk AB, Sweden) with 20 mW output power at room temperature. The thermal conductivity data were obtained using the anisotropic method. FLIR E60 infrared thermography was performed to capture the thermographic photo (FLIR Company, USA) with a 0.05 °C resolution. The radial and axial directions of the sample were tested on a hot plate and the temperature range was set from 16 to 70 °C.

Limited oxygen index (LOI)

The LOI was measured using the S/N710 oxygen index meter (Santon Redcroft Co. UK), according to the ASTM 2863 standard method. The aerogel size was controlled at 80 × 10 × 10 mm; the instrument was equipped with top surface ignition.

Cone calorimetry

Cone calorimetry (FireTEC, USA) was used to measure the combustion properties of squared aerogels (100 × 100 × 5 mm) according to the ASME E1354 standard method. The test parameters were collected including the ignited time, peak rate and average rate of heat release, total heat released and toxic gas concentration. The test result was repeatedly measured four times to ensure precise data.

Vertical burning tests (UL94)

The burning performance of the aerogel was analyzed with the UL94 standard vertical burning test. The length and diameter of the cylindrical aerogel were 120 mm and 10 mm, respectively.

Acknowledgements

References

1 P. H. Shaikh, N. B. M. Nor, P. Nallagownden, I. Elamvazuthi and T. Ibrahim, *Renewable Sustainable Energy Rev.*, 2014, **34**, 409–429.

2 D. Ürge-Vorsatz, L. F. Cabeza, S. Serrano, C. Barreneche and K. Petrichenko, *Renewable Sustainable Energy Rev.*, 2015, **41**, 85–98.

3 A. B. Morgan and J. W. Gilman, *Fire Mater.*, 2013, **37**, 259–279.

4 A. Briga-Sá, D. Nascimento, N. Teixeira, J. Pinto, F. Caldeira, H. Varum and A. Paiva, *Constr. Build. Mater.*, 2013, **38**, 155–160.

5 A. Kumar and B. M. Suman, *Build. Environ.*, 2013, **59**, 635–643.

6 O. Kaynakli, *Renewable Sustainable Energy Rev.*, 2012, **16**, 415–425.

7 K. Wei, C. Lv, M. Chen, X. Zhou, Z. Dai and D. Shen, *Energy Buildings*, 2015, **87**, 116–122.

8 S. Medved, B. Lesar, E. M. Tudor and M. Humar, *For. Prod. J.*, 2015, **65**, S54–S54.

9 R. Dietz, F. F. Riget, C. Sonne, E. W. Born, T. Bechshoft, M. A. McKinney, R. J. Drimmie, D. C. Muir and R. J. Letcher, *Environ. Int.*, 2013, **59**, 494–500.

10 S. Brehme, T. Köppl, B. Schartel and V. Altstädt, *e-Polym.*, 2014, **14**, 193–208.

11 H. Zhu, W. Luo, P. N. Ciesielski, Z. Fang, J. Y. Zhu, G. Henriksson, M. E. Himmel and L. Hu, *Chem. Rev.*, 2016, **116**, 9305–9374.

12 H. Zhu, S. Parvinian, C. Preston, O. Vaaland, Z. Ruan and L. Hu, *Nanoscale*, 2013, **5**, 3787–3792.

13 H. Zhu, S. Zhu, Z. Jia, S. Parvinian, Y. Li, O. Vaaland, L. Hu and T. Li, *Proc. Natl. Acad. Sci. U. S. A.*, 2015, **112**, 8971–8976.

14 K. Zhou, W. Yang, G. Tang, B. Wang, S. Jiang, Y. Hu and Z. Gui, *RSC Adv.*, 2013, **3**, 25030.

15 D. Wang, L. Song, K. Zhou, X. Yu, Y. Hu and J. Wang, *J. Mater. Chem. A*, 2015, **3**, 14307–14317.

16 J. L. Verble, T. J. Wietling and P. R. Reed, *Solid State Commun.*, 1972, **11**, 941–944.

17 M. A. Worsley, S. J. Shin, M. D. Merrill, J. Lenhardt, A. J. Nelson, L. Y. Woo, A. E. Gash, T. F. Baumann and C. A. Orme, *ACS Nano*, 2015, **9**, 4698–4705.

18 X. Geng, W. Sun, W. Wu, B. Chen, A. Al-Hilo, M. Benamara, H. Zhu, F. Watanabe, J. Cui and T. P. Chen, *Nat. Commun.*, 2016, **7**, 10672.

19 H. Dong, J. F. Snyder, K. S. Williams and J. W. Andzelm, *Biomacromolecules*, 2013, **14**, 3338–3345.

20 X. Zhang, L. Chen, T. Yuan, H. Huang, Z. Sui, R. Du, X. Li, Y. Lu and Q. Li, *Mater. Horiz.*, 2014, **1**, 232–236.

21 D. J. Sathe, P. A. Chate, S. B. Sargar, S. V. Kite and Z. D. Sande, *J. Mater. Sci.: Mater. Electron.*, 2016, **27**, 3834–3838.

22 K. Zhang, L. Zong, Y. Tan, Q. Ji, W. Yun, R. Shi and Y. Xia, *Carbohydr. Polym.*, 2016, **136**, 121–127.

23 G. Chinga-Carrasco, *Nanoscale Res. Lett.*, 2011, **6**, 417.

24 H. Dong, J. F. Snyder, D. T. Tran and J. L. Leadore, *Carbohydr. Polym.*, 2013, **95**, 760–767.

25 H. Huang, P. Chen, X. Zhang, Y. Lu and W. Zhan, *Small*, 2013, **9**, 1397–1404.

26 H. Huang, S. Lü, X. Zhang and Z. Shao, *Soft Matter*, 2012, **8**, 4609–4615.

27 S. M. Jung, H. Y. Jung, M. S. Dresselhaus, Y. J. Jung and J. Kong, *Sci. Rep.*, 2012, **2**, 849.

28 K. S. Sing and R. T. Williams, *Adsorpt. Sci. Technol.*, 2004, **22**, 773–782.

29 F. Jiang and Y.-L. Hsieh, *J. Mater. Chem. A*, 2014, **2**, 6337.

30 S. Cadot, O. Renault, M. Frégnaux, D. Rouchon, E. Nolot, K. Szeto, C. Thieuleux, L. Veyre, H. Okuno and F. Martin, *Nanoscale*, 2017, **9**, 538–546.

31 M. S. Cross, P. A. Cusack and P. R. Hornsby, *Polym. Degrad. Stab.*, 2003, **79**, 309–318.

32 Q. Wang, J. Guo, D. Xu, J. Cai, Y. Qiu, J. Ren and L. Zhang, *Cellulose*, 2015, **22**, 3799–3810.

33 J. Zhao, X. Zhang, R. Tu, C. Lu, X. He and W. Zhang, *Cellulose*, 2014, **21**, 1859–1872.

34 B. Wicklein, A. Kocjan, G. Salazar-Alvarez, F. Carosio, G. Camino, M. Antonietti and L. Bergstrom, *Nat. Nanotechnol.*, 2015, **10**, 277–283.

35 B. Notario, J. Pinto, E. Solorzano, J. A. de Saja, M. Dumon and M. A. Rodríguez-Pérez, *Polym.*, 2015, **56**, 57–67.

36 T. L. Bergman and F. P. Incropera, *Introduction to heat transfer*, John Wiley & Sons, 2011.

37 K. Zhou, G. Tang, S. Jiang, Z. Gui and Y. Hu, *RSC Adv.*, 2016, **6**, 37672–37680.

38 R. E. Anderson, J. Guan, M. Ricard, G. Dubey, J. Su, G. Lopinski, G. Dorris, O. Bourne and B. Simard, *J. Mater. Chem.*, 2010, **20**, 2400.

39 X. Feng, W. Xing, L. Song and Y. Hu, *J. Mater. Chem. A*, 2014, **2**, 13299.

40 Y. Li, H. Zhu, F. Shen, J. Wan, S. Lacey, Z. Fang, H. Dai and L. Hu, *Nano Energy*, 2015, **13**, 346–354.